Breaking of Internal Kelvin Waves Shoaling on a Slope

Nakayama, K. ; Sato, T. ; Tani, K. ; Boegman, L. ; Fujita, I. ; Shintani, T.

(Citation)
Journal of Geophysical Research: Oceans,125(10):e2020JC016120

(Issue Date)
2020-10

(Resource Type)
journal article

(Version)
Version of Record

JGR Oceans

RESEARCH ARTICLE
10.1029/2020JC016120

Breaking of Internal Kelvin Waves Shoaling on a Slope

K. Nakayama[1], T. Sato[2], K. Tani[1], L. Boegman[3], I. Fujita[1], and T. Shintani[4]

[1]Graduate School of Engineering, Kobe University, Kobe, Japan, [2]Energy System and Plant Engineering Company, Kawasaki Heavy Industries, Ltd., Kobe, Japan, [3]Department of Civil Engineering, Queen's University at Kingston, Kingston, Ontario, Canada, [4]Faculty of Urban Environmental Sciences, Tokyo Metropolitan University, Hachioji, Japan

Key Points:
- A residual jet was shown to occur at the lateral wall of a cyclonically propagating internal Kelvin wave breaking over a uniform slope
- The residual jet occurred under a geostrophic balance and generated an oblique downdraft running down the slope, due to Coriolis
- An equation was formulated for estimating the residual current due to the residual jet

Correspondence to:
K. Nakayama,
nakayama@phoenix.kobe-u.ac.jp

Citation:
Nakayama, K., Sato, T., Tani, K., Boegman, L., Fujita, I., & Shintani, T. (2020). Breaking of internal Kelvin waves shoaling on a slope. *Journal of Geophysical Research: Oceans*, *125*, e2020JC016120. https://doi.org/10.1029/2020JC016120

Received 4 FEB 2020
Accepted 25 SEP 2020
Accepted article online 29 SEP 2020

Abstract In stratified flow, breaking of internal waves over slopes induces resuspension of bottom sediments and transport of mass. When internal waves shoal and break, flow dynamics and mass transport differ significantly according to whether the Coriolis force is included or neglected. Despite its importance, the currents generated by breaking internal Kelvin waves remain uninvestigated. Therefore, this study considers breaking of internal waves over a uniform slope under Coriolis with equivalent upper- and lower-layer depths. Laboratory experiments, using a 6.0-m rotating tank, were undertaken to visualize currents using particle image velocimetry. Experimental data validated a three-dimensional fluid dynamics model, in which a phase-averaged velocity (residual jet) was simulated to occur at the lateral wall (to the right) of the progressive internal Kelvin waves in the breaking zone, with the generation of an oblique downslope return flow (downdraft) under Coriolis. The geostrophic balance drove the residual jet, and the equation for estimating the residual current, due to the jet, was formulated and was discussed by referring a coastal jet in Lake Erie. The results provide insight on mass transport in lakeshore and coastal zones.

Plain Language Summary The key idea of the present study is the "residual jet" which occurs at the lateral wall on the right side of the progressive internal Kelvin waves due to breaking over a uniform slope. We conducted laboratory experiments by using a rotating tank, and internal Kelvin wave breaking was visualized by using particle image velocimetry (PIV) method. Also, using a three-dimensional fluid dynamics model, a residual jet was demonstrated to occur with the generation of an oblique downdraft running down the slope under Coriolis, which was verified through the laboratory experiments. We found that the geostrophic balance drives a residual jet, and the equation for estimating the residual current, due to the jet, was formulated and was discussed by referring a coastal jet in Lake Erie. Therefore, the paper will provide the oceanography communities with a new understanding of the effect of internal Kelvin wave breaking, and the associated residual currents, on long-term mass transport.

1. Introduction

In lakes and the ocean, breaking of internal waves over slopes plays an important role in resuspension and transport of mass (e.g., Boegman & Stastna, 2019; Lamb, 2014; Wüest & Lorke, 2003). When internal waves shoal and break, the breaking induces resuspension of bottom sediments (Gloor et al., 1994; Moum et al., 2003; Pierson & Weyhenmeyer, 1994; Steinman et al., 1997). Residual currents, from internal wave shoaling, cause long-term sediment transport, which affects biogeochemistry in coastal areas (Aghsaee & Boegman, 2015; Boegman & Ivey, 2009; Davis & Monismith, 2011; Hosegood et al., 2004; Inall, 2009; Klymak & Moum, 2003; Scotti & Pineda, 2004; Walter et al., 2012).

For example, Pineda (1994) found that internal bores, from breaking of internal waves, periodically influenced onshore transport of neustonic larvae in Southern California. Sandstrom and Elliott (1984) suggested that the occurrence of several large wave-shoaling events per tidal cycle was sufficient to supply the required nutrients to the euphotic zone on the Scotian Shelf (Helfrich, 1992). Reeder et al. (2011) observed sand waves (amplitudes ≤16 m and wavelengths ≤350 m) on the continental formed by episodic shoaling of extreme internal solitary waves (ISWs) (>100-m amplitudes) during each lunar cycle. ISW breaking dynamics, including the formation of vortex cores during breaking (Derzho & Grimshaw, 1997), is important for long-term mass transport (Lamb, 2002). The flow dynamics and mass transport will differ significantly according to whether the Coriolis force is included or neglected (Asplin et al., 1999; Csanady, 1967; de la

Fuente et al., 2008; Grimshaw & Helfrich, 2012; Hamblin, 1978; Helfrich, 2007; Maxworthy, 1983; Melville et al., 1990; Mortimer, 1952).

Prior research that considers breaking of internal waves over a slope without Coriolis has demonstrated that the generation of high-frequency internal waves, accompanying the change in water depth over the slope, plays an important role in the type of internal wave breaking (Helfrich et al., 1984; Helfrich & Melville, 2006; Nakayama et al., 2012). Boegman et al. (2005a) also showed that degeneration, from a low-frequency internal seiche to high-frequency ISWs, is a significant factor, generating dynamic breaking in laboratory experiments using a tilting tank. Similarly, the laboratory experiments and analysis using the mKdV model by Horn et al. (2000, 2001, 2002) and the analysis using the fully nonlinear and strongly dispersive internal wave equations by Nakayama, Kakinuma, and Tsuji (2019) showed that degeneration from low- to high-frequency internal waves, through fission, will occur readily over a mild slope of $<$ ~0.05 (Nakayama, Sato, et al., 2019).

Bourgault et al. (2014) found that mass transport from the breaking of ISWs over a slope differs according to the type of breaking. Boegman et al. (2005a) proposed an internal form of the Iribarren number, modified after Galvin (1968), and three types of breaking for ISWs in a two-layer laboratory system: spilling, plunging, and collapsing breakers. Aghsaee et al. (2010) extended this work to include fission and demonstrated that computational results could be classified using bottom slope and wave slope. Sutherland et al. (2013) performed additional experiments and reconciled differences between the prior laboratory and numerical work, classifying both in terms of the internal Iribarren number. Nakayama, Sato, et al. (2019) proposed a new wave Reynolds number which can delineate plunging and collapsing breakers based on bottom slope and wave slope.

There are many studies related to the breaking of internal waves in a two-layer system when the depths of the upper and lower layers are equivalent (e.g., Nakayama & Imberger, 2010). Nakayama and Imberger (2010) showed, in laboratory experiments, that collapsing breakers predominate regardless of layer depth, specific density ratios, and wave slope. In general, collapsing breakers occur when the depths of the upper and lower layers are the same (over the flat bottom) using the critical depth, which is obtained from the nonlinear term of the KdV equation (Nakayama, Sato, et al., 2019).

It has long been known that internal wave dynamics vary greatly when Coriolis effects are included. Helfrich (2007) successfully evaluated the decay of internal Kelvin waves (IKWs), by assuming that there is no change in the transverse direction to investigate ISWs with rotation in the ocean (Grimshaw et al., 2014). As the other example of ISWs with rotation, Shimizu and Nakayama (2017) also showed that bow-shaped ISWs propagate under the influence of the Earth's rotation (Grimshaw et al., 2013), and soliton resonance for ISWs was found to occur with rotation. Maxworthy (1983) demonstrated that the transverse scales of the topography are not negligible for internal waves with rotation, in the oceanographic applications to sea straits and the continental shelves. Similarly, Melville et al. (1989, 1990) investigated the amplitude decay of IKWs, propagating along the lateral wall of a channel.

The investigation of IKWs, with the presence of a lateral wall boundary, is of interest when determining long-term mass transport in the coastal boundary layer (Stocker & Imberger, 2003; Ulloa et al., 2015; Wake et al., 2005). For example, Antenucci and Imberger (2001) showed the importance of IKWs within the littoral zone of Lake Kinneret. Csanady (1975) found, through observation and theory, that IKW motion is one of the critical factors controlling the coastal jet in Lake Ontario (Csanady, 1972a, 1972b). Valipour et al. (2019) investigated nearshore/offshore connectivity resulting from IKWs in Lake Erie. For IKWs, in the presence of a lateral wall boundary, steepening occurs (Boegman et al., 2003), but production mechanisms of ISWs remain unclear with energy being lost to internal Poincaré waves (de la Fuente et al., 2008; Mortimer, 2004). Moreover, research on steady-state ISWs under Coriolis is lacking (Maxworthy, 1983; Melville et al., 1989, 1990; Renouard et al., 1987); however, IKWs will be preferentially generated over ISWs, for small-amplitude waves, when the depths of the upper and lower layers are equivalent and in the presence of a lateral wall boundary (Boegman et al., 2005b; Gill, 1982).

Therefore, as a first step to investigate breaking of internal waves over a slope considering Coriolis effects, it is necessary to study IKWs generated along the lateral wall when the depths of the upper and lower layers are equivalent. For the same case without Coriolis, a collapsing breaker will predominate over a uniform slope. A residual undertow, due to downdraft, will occur that drives an offshore bottom current from the littoral zone

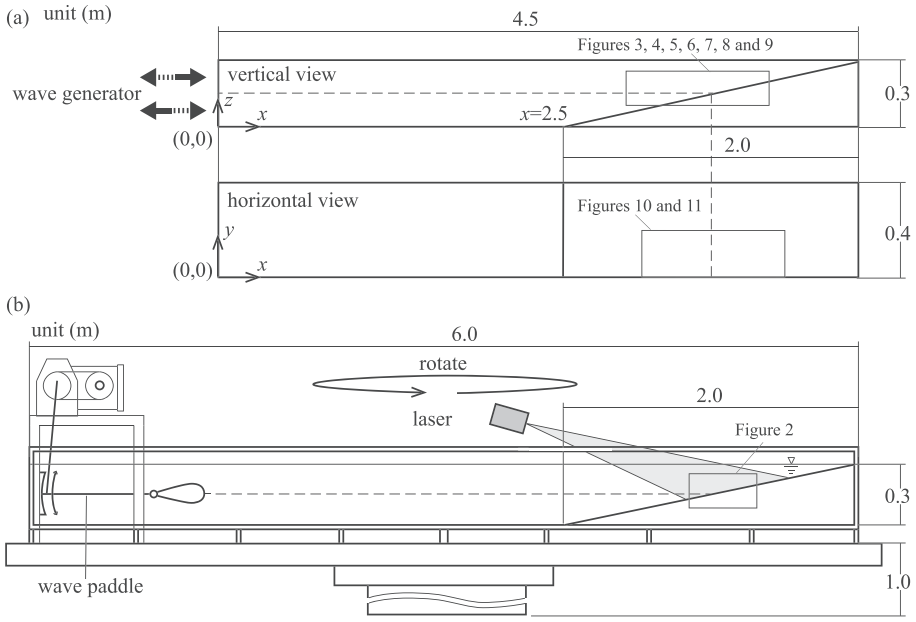

Figure 1. Schematic diagram of the (a) computational domain and (b) laboratory experiment tank.

below the density interface and induces long-term mass transport (Nakayama & Imberger, 2010). However, an IKW progresses with maximum amplitude at the lateral wall, and the amplitude decreases significantly in the wall-normal direction. Therefore, when Coriolis effects are considered, the mass transport mechanisms will likely differ from those revealed by Nakayama and Imberger (2010).

This study investigates how residual currents are generated when the water depths of the upper and lower layer are equivalent under Coriolis effects, using both laboratory experiments and numerical simulations. In the laboratory experiments, a 6.0-m rotating tank was visualized using particle image velocimetry (PIV). In the numerical simulations, the Fantom model shown to have high reproducibility and accuracy in internal wave breaking by Nakayama et al. (2012) and Nakayama, Kakinuma, and Tsuji (2019) was applied to investigate the types of breaking of IKWs and residual currents under varying Coriolis conditions.

2. Method

2.1. Laboratory Experiments

Laboratory experiments were carried out using a rotating tank with a length of 6.0 m, a width of 0.4 m, and water depth of 0.3 m. The tank was mounted on a rotating table with a width of 3.0 m and a length of 6.0 m at the height of 1.0 m from the ground (Figure 1b). The bottom slope was 0.3 m/2.0 m. By setting the length of the wave paddle to 0.7 m and the length of the nose-like airfoil to 0.5 m, the distance from the wave generation site to the end of the slope was 4.8 m. IKWs were generated by oscillating the wave paddle, which was first designed by Thorpe (1978) and used in the previous study by Nakayama and Imberger (2010). The nose-like airfoil was attached to prevent mixing adjacent to the area where the pycnocline intersects the airfoil. Density stratification was produced by slowly injecting saltwater of $\rho_2 = 1{,}020$ kg m^{-3} from two 0.03-m diameter holes in the bottom of the tank after filling with fresh water of $\rho_1 = 1{,}000$ kg m^{-3} to the desired layer depth. Since IKWs have been shown to progress stably when the ratio of the upper- and lower-layer depths is 1, equivalent 0.15-m depths were specified for each layer. The thickness of the pycnocline was 0.02 m. In all experiments, the tank was spun-up for 30 min, so as to be in the œsolid-body rotation. From the layer thickness (= 0.15 m), viscosity (= 10^{-6} m^2 s^{-1}), and the Coriolis coefficient (= $4\pi/30$ s^{-1}), the time-scale characterizing spin-down is estimated to be 756 s, showing that 30 min is sufficient. To make comparisons under the same conditions, the total cross-sectional flux, for producing IKWs, was made equivalent in all cases of the laboratory experiments and numerical simulations.

Table 1
Computational Conditions

	f_C (s^{-1})	λ_I (m)	a_0 (m)	η_{B0} (m)	u_B (m s^{-1})
Case A	—	—	0.010	—	—
Case B1	4π/20	0.19	0.024	0.018	0.029
Case B2	4π/30	0.29	0.018	0.015	0.025
Case B3	4π/40	0.39	0.016	0.013	0.021
Case B4	4π/80	0.77	0.013	0.009	0.015
Case B5	4π/160	1.54	0.011	0.008	0.011

Note. The upper- and lower-layer depths were 0.15 and 0.15 m, respectively, ε was 0.02, the period of an IKW was 10.0 s, and the width of the tank was 0.4 m.

For the laboratory experiments, case 'A' without Coriolis effects and case 'B2' with a Coriolis coefficient of $4\pi/30$ s^{-1} were carried out (Table 1). The period of IKWs, in both cases, was unified at 10.0 s, which corresponds to a wavelength of 1.2 m using a longwave celerity. The amplitude of internal waves in Case A was set to 0.01 m, and the same total cross-sectional flux was given in Case B2. To verify the computational results, the flow velocity was determined using PIV. The flow field was illuminated over a horizontal length of 0.40 m and vertical height of 0.15 m on the right side of the IKW propagation direction using a Yag Laser (JAPAN LASER CORPORATION, DPGL-2W) with a sheet thickness of 0.005 m (Figure 1b). The video camera (CASIO EX-100 Pro) resolution was 3,840 × 2,160 with a 30 s^{-1} frame rate (Fujita, 2002; Fujita & Maruyama, 2002). The flow was seeded with nylon crushed particles with a diameter of 80 μm and a specific gravity of 1.02. Since internal waves reach the slope 50 s after generation, PIV measurements were performed for 70 s (from 50 to 120 s).

2.2. Numerical Simulations

A three-dimensional nonhydrostatic model, Fantom, was used to analyze the breaking of internal Kevin waves shoaling on the uniform slope. Fantom is an object-oriented parallel computing model that has been applied to investigate not only real scale phenomena (Maruya et al., 2010; Nakamoto et al., 2013; Nakayama et al., 2014, 2016) but also laboratory-scale phenomena (Nakayama et al., 2012, 2020; Nakayama, Kakinuma, and Tsuji, 2019). Fantom is based on Direct numerical simulation (DNS) as well as a generic length scale (GLS) equation model (Jones & Launder, 1972; Umlauf & Burchard, 2003), with a partial cell scheme used here to represent the uniform bottom slope in the z coordinate bathymetry (Adcroft et al., 1997). Nakayama and Imberger (2010) computed a Kolmogorov scale of 0.56 mm, during collapsing breakers occurs over a uniform slope in a laboratory experiment, which is similar to Case A. The vertical grid spacings, in this study, of 2.0 mm over the slope is 3.6 of the Kolmogorov scale and well within the grid limits for DNS (Moin & Mahesh, 1998). Arthur and Fringer (2014) further demonstrated that 9 times the Kolmogorov scale is sufficient for ISW breaking. Therefore, a subgrid-scale closure scheme is not required in the present study.

The size of the computational domain was 4.5 m in length and 0.4 m in height, with a 0.3-m water depth and a slope of 0.3 m/2.0 m (Figure 1a). To be consistent with laboratory experiments, we applied an initial hyperbolic tangent stratification:

$$\rho(z) = \rho_1 + \frac{\Delta\rho}{2}\left(1 + \tanh\frac{z - h_2}{0.5\alpha}\right) \tag{1}$$

where z is the upward positive vertical coordinate with an origin at the equilibrium water surface, $h_2$is the lower-layer thickness, $\rho_1$is the density of the upper layer, $\Delta\rho$ is the density difference between the upper and lower layers, and α (= 0.02 m) is the thickness of the pycnocline.

We considered the case with a lower-layer density ρ_2 = 1,020 kg m^{-3} and an upper-layer density ρ_1 = 1,000 kg m^{-3}. IKWs were initialized with the theoretical solution of the flux with a phase of π in the upper and lower layers (left of Figure 1a). As in the laboratory experiments, the amplitude of IKWs in Case A, without Coriolis, was set to 0.01 m and the other computations with Coriolis were performed by giving the same total cross-section flux in all cases:

$$U_{upper} = \frac{\varepsilon g a_0}{c_0}\exp\left(-\frac{f_C}{c_0}y\right)\sin\left(\frac{2\pi t}{t_i}\right) \tag{2}$$

$$U_{lower} = -U_{upper} \tag{3}$$

$$\varepsilon = \frac{\rho_2 - \rho_1}{\rho_2} \tag{4}$$

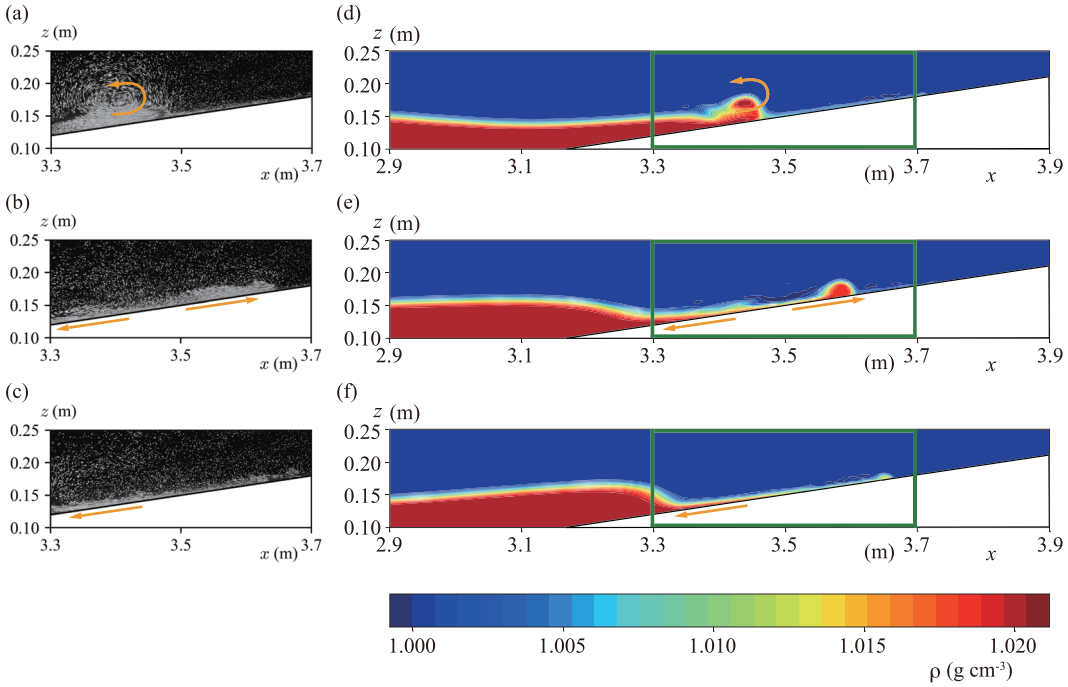

Figure 2. PIV particle and density distributions without the Coriolis effect under Case A at $y = 0.005$ m. PIV particle distributions in the laboratory experiments at (a) $t = 54$ s, (b) $t = 58$ s, and (c) $t = 60$ s. Density distributions in the numerical simulations at (d) $t = 54$ s, (e) $t = 58$ s, and (f) $t = 60$ s. Green squares indicate the PIV analysis region corresponding to Figures 2a–2c.

$$a_0 = a_m \frac{B}{\lambda_I} \frac{1}{1 - \exp(-B/\lambda_I)} \tag{5}$$

where U_{upper} is the flux in the upper layer, a_0 is the amplitude of an IKW at the lateral wall, g is the gravitational acceleration, c_0 is the celerity of IKW, f_C is the Coriolis parameter, y is the width coordinate, t is the time, $t_i$is the period of the IKW, a_m is the amplitude without Coriolis (= 0.01 m), B is the width of the tank, U_{lower} is the flux in the lower layer, and λ_I is the inertial deformation radius (= c_0/f_C).

The horizontal mesh size in the vicinity of the wave generator was 0.04 m, with a mesh of 0.005 m given on the bottom slope where the breaking of IKWs occurs. The vertical mesh was 0.01 m at the upper and lower ends and 0.002 m over the bottom slope. The computational time step was 0.01 s, which corresponds to a CFL condition of 0.24 based on a longwave celerity and the smallest mesh size. A free surface was applied to the top boundary, and no-slip conditions were given on the bottom and lateral boundaries. To investigate the effect of the Coriolis force, five different conditions were given, with Coriolis coefficient of $4\pi/20$, $4\pi/30$, $4\pi/40$, $4\pi/80$, and $4\pi/160$ s^{-1} (Table 1). As the long wave celerity was estimated to be 0.121 m s^{-1}, the minimum and maximum inertial deformation radii were 0.19, 0.29, 0.39, 0.77, and 1.54 m for Cases B1 to B5, respectively. The total computational time was set to 100 s, which reproduced the IKW reflecting from the slope and reaching the wave generator.

3. Results

3.1. Laboratory Experiments

To visualize the internal wave motion, a sequence of five images was superimposed (Figures 2a–2c and Figures 3a–3c). For example, Figure 2a was made by superimposing the five particle images from 54 to 54 + 4/30 s with an interval of 1/30 s, which enables the particle trajectory streaks to be visualized (shown by the orange arrow). The location of the visualization was at $y = 0.005$ m, due to the thickness of a laser sheet. In the absence of the Coriolis force, the particle motions revealed a downdraft (Figure 2c), with vertical circulation formed by the shoaling front of the internal wave (Figure 2a), which ran up the slope

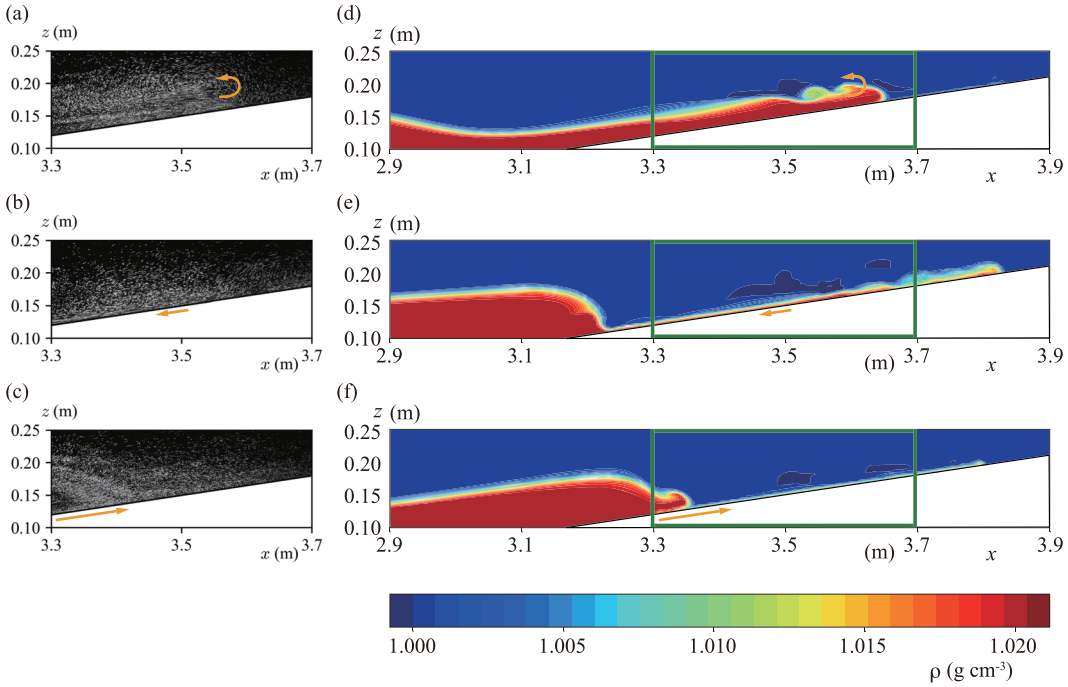

Figure 3. PIV particle and density distributions with the Coriolis coefficient of $4\pi/30$ (s^{-1}) under Case B2A at $y = 0.005$ m. PIV particle distributions in the laboratory experiments at (a) $t = 54$ s, (b) $t = 58$ s, and (c) $t = 60$ s. Density distributions in the numerical simulations at (d) $t = 54$ s, (e) $t = 58$ s, and (f) $t = 60$ s. Green squares indicate the PIV analysis region corresponding to Figures 3a–3c.

(Figure 2b). The breaking type was confirmed to be a collapsing breaker by comparing with the collapsing breaker shown in Nakayama and Imberger (2010; their Figure 6). We confirmed that a collapsing breaker occurred in the different vertical cross section, and there was no change in a breaking type in the spanwise direction. In contrast, when Coriolis was included, no strong downdraft over the slope was evident at $y = 0.005$ m (Figure 3c). The vertical circulation at the front was also weak compared to the no

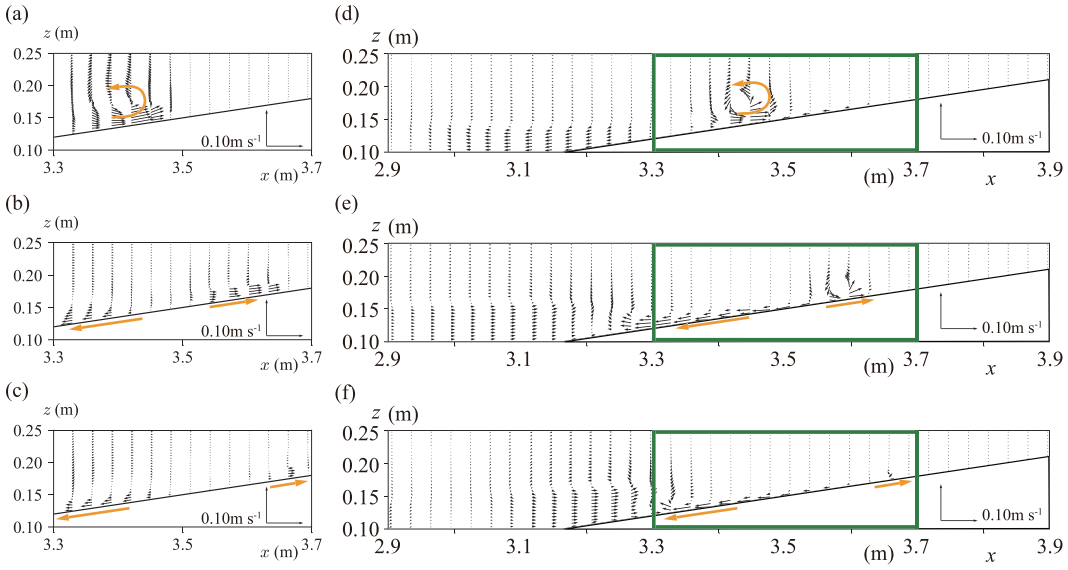

Figure 4. Velocity vectors without the Coriolis effect under Case A at $y = 0.005$ m. PIV analysis in the laboratory experiments at (a) $t = 54$ s, (b) $t = 58$ s, and (c) $t = 60$ s. Numerical simulations at (d) $t = 54$ s, (e) $t = 58$ s, and (f) $t = 60$ s. Green squares indicate the PIV analysis region corresponding to Figures 4a–4c.

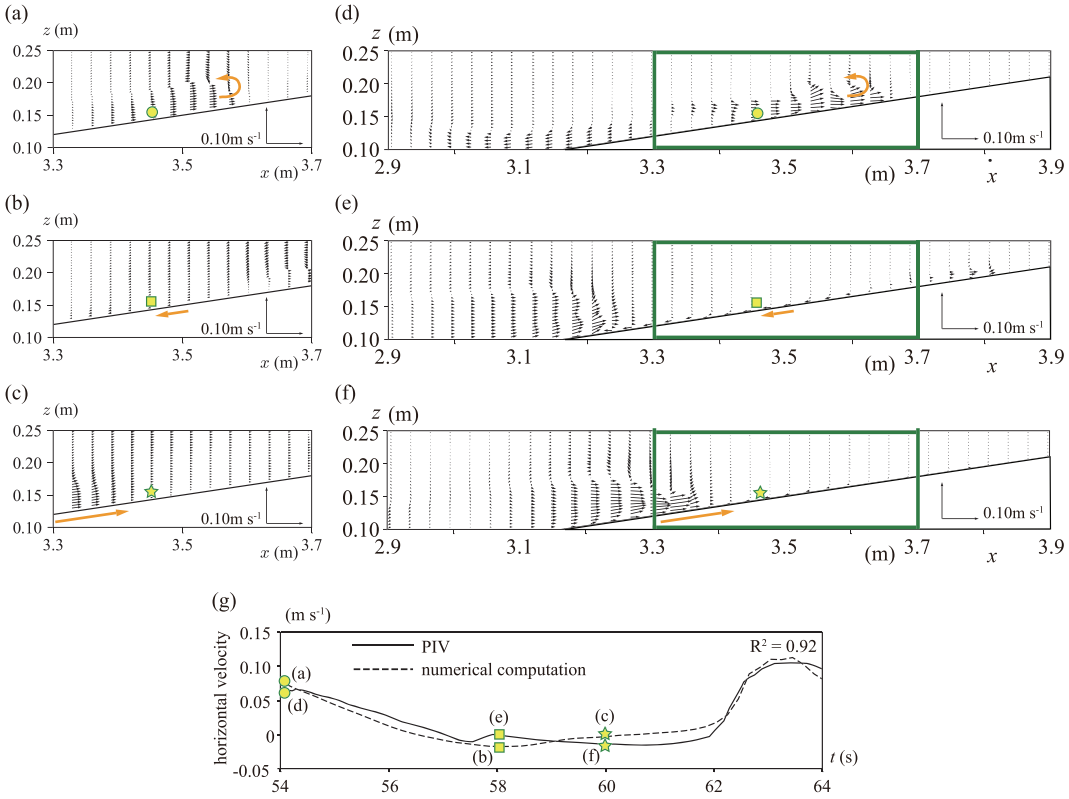

Figure 5. Velocity vectors with the Coriolis coefficient of $4\pi/30\ s^{-1}$ under Case B2 at $y = 0.005$ m. PIV analysis in the laboratory experiments at (a) $t = 54$ s, (b) $t = 58$ s, and (c) $t = 60$ s. Numerical simulations at (d) $t = 54$ s, (e) $t = 58$ s, and (f) $t = 60$ s. Green squares indicate the PIV analysis region corresponding to Figures 5a–5c. (g) Horizontal velocity at $x = 3.45$ m and $z = 0.15$ m.

Coriolis case (Figure 3a) because the downdraft strengthened the front circulation in the case of no Coriolis (Figure 2a). The type of breaking, within the $y = 0.005$ m plane, was similar to a collapsing-surging breaker, which has a weaker vertical circulation at the front.

PIV was performed using the particle images (Figures 2a–2c and Figures 3a–3c). Following the particle images, strong downdraft was found to occur without Coriolis (Figure 4c). As a result of the collision of the downdraft and the front, strong vertical circulation was generated (Figure 4a). The front then ranup over the slope and separated as a part of the downdraft (Figure 4b). When Coriolis was included, the downdraft did not form (Figure 5c). Thus, the front was revealed to have less vertical circulation and the runup distance was larger than the no Coriolis case because baroclinic energy converged on the lateral wall in the case with Coriolis (Figures 4a and 5a). Overall, at the lateral wall, the velocity with Coriolis was shown to be larger than the no Coriolis case. In the laboratory experiments, accurate visualization was only carried out at $y = 0.005$ m. It was difficult to visualize inside the rotating tank due to the presence of large spanwise velocities perpendicular to the visualization plane, resulting in out-of-plane motion through the laser sheet. Therefore, we relied on the numerical simulations to further investigate breaking of IKWs under different Coriolis conditions.

3.2. Numerical Simulations

Collapsing breakers occurred at $y = 0.005$ m without Coriolis (Case A), as in the laboratory experiments (Figures 2d–2f). During shoaling, the downdraft from the previous wave established a circulation at the internal wavefront, which ranup over the slope, establishing a downdraft. Again, in Case B2 when the IKW ranup over the slope, the breaking type was found to be collapsing-surging at $y = 0.005$ m and the thickness of the front was smaller than the no Coriolis case because downdraft was not evident at $y = 0.005$ m (Figures 3d–3f). Good agreement was found between the DNS and velocity vectors from the laboratory experiments, for cases both with and without Coriolis (Figures 4 and 5). The time series of the horizontal

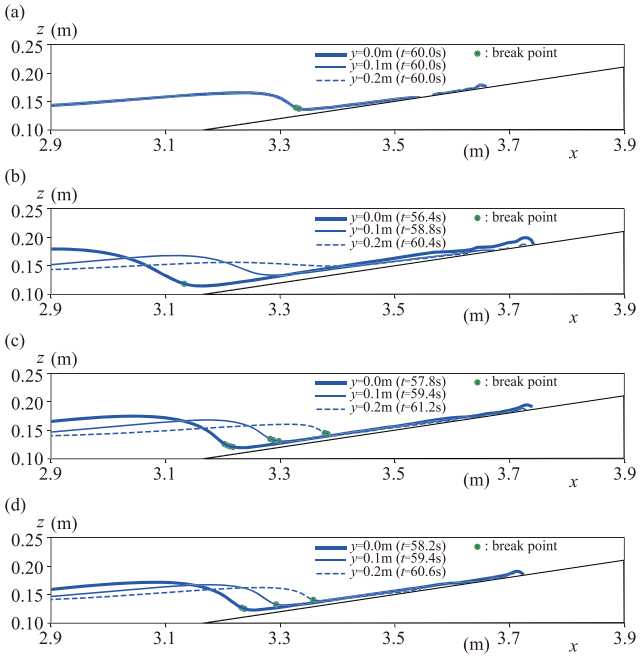

Figure 6. Spanwise pycnocline displacement when breaking points appear at the lateral wall (thick solid lines), at $y = 0.1$ m (thin solid lines) and $y = 0.2$ m (broken lines). Green circles indicate breaking points. (a) Case A: no Coriolis effect, (b) Case B1: Coriolis coefficient of $4\pi/20$ s^{-1}, (c) Case B2: Coriolis coefficient of $4\pi/30$ s^{-1}, and (d) Case B3: Coriolis coefficient of $4\pi/40$.

velocity, around the breaking zone at $x = 3.45$ m with $z = 0.15$ m, yielded a correlation coefficient, $R^2 = 0.92$ showing the quantitative performance of the model relative to the laboratory experiments (Figure 5). In Case B2, with a Coriolis coefficient of $4\pi/30$ s^{-1}, there was no clear evidence of a downdraft at $y = 0.005$ m after the IKW ranup over the slope, which suggests that the lower layer fluid transported upslope moved in the spanwise direction, during wave breaking, due to Coriolis with a return flow at a different y position. Furthermore, since the inertial deformation radius was 0.29 m, that shorter than the wavelength of IKWs, it was expected that Coriolis enhanced mass transport in the spanwise direction. The thickness of the Ekman boundary layer was estimated about 0.002 to 0.003 m for the strong Coriolis cases, Cases B1 to B3. Therefore, it is expected that there is no substantial influence of the bottom Ekman boundary layer on the breaking of IKWs over a uniform slope.

To investigate how Coriolis affected breaking of IKWs, we compared the spanwise pycnocline displacement for Case A (without Coriolis) and Cases B1 to B3 (with Coriolis coefficients of $4\pi/20$, $4\pi/30$, and $4\pi/40$ s^{-1}; Figure 6). In Case B1, where the Coriolis coefficient was the maximum and the amplitude at the lateral wall was the largest, the runup distance was at its maximum, and the breaker type was collapsing-surging (Figure 6b). The definition of breaking point used in Nakayama et al. (2012) was applied (vertical pressure gradient is zero), to investigate the influence of Coriolis on breaking (Figure 6). When Coriolis was neglected, breaking occurred at the point where the downdraft collided with the front; as shown in Nakayama et al. (2012; their Figure 6a). For Case B, where Coriolis was considered, the breaking point moved in the upslope direction as y increased. Since the inertial deformation radius was 0.19 m in Case B1, the amplitude became too small to break over the slope at $y = 0.2$ m (Figure 6b). In contrast, for Cases B2 and B3, because the internal deformation radii were 0.29 and 0.39 m, the IKW was found to break over the slope at $y = 0.2$ m. The location of the breaking point in Case B3 was similar to the no Coriolis case, which suggests that Coriolis changes the breaking type in the spanwise direction. Cases B4 and B5 were omitted in Figure 6, because when the Coriolis coefficient is smaller and the internal deformation radius is larger, these showed the same tendency as Case B3. In particular, in Case B5 with the smallest Coriolis coefficient, we could confirm the apparent occurrence of vertical circulation at the front, which can be seen under the no Coriolis case. It should be noted that the time is not fixed in Figure 6 because we picked up the time when the breaking occurred for each spanwise pycnocline displacement.

3.3. Residual Current Analysis

To investigate long-term mass transport, phase-averaged density distributions and velocities were calculated adjacent to the lateral wall over three-wave periods from the third to the fifth wave after the IKW reached the slope. The phase-averaged pycnocline became thicker in all Coriolis cases compared to the no Coriolis case (Figure 7). The maximum thickness of the phase-averaged pycnocline occurred in Case B1, where the amplitude at the lateral wall was the maximum among all cases (Table 1). The thickness of the phase-averaged pycnocline decreased with the amplitude at the lateral wall (Figure 7). Cases B2 and B4 were omitted in Figure 7 because they showed the same rate of decrease of the phase-averaged pycnocline thickness from Case B1 to Case B5. Since energy damping due to the breaking of the IKW at the lateral wall becomes larger as the amplitude increases, there is the possibility that the thickness of the phase-averaged pycnocline increases from Case B5 to Case B1 is due to the strength of turbulence causing mixing during the breaking of IKWs.

Residual currents were obtained by averaging velocities over three-wave periods from the third to the fifth wave after the IKW reached the slope, which corresponds to Eulerian averages (Figure 8). Eulerian averages (residual currents) were revealed to correspond to Lagrangian transport under the periodic wave conditions (Nakayama & Imberger, 2010). In the absence of Coriolis (Case A) an upslope residual current was generated above the phase-averaged pycnocline and a downslope return flow beneath the phase-averaged pycnocline

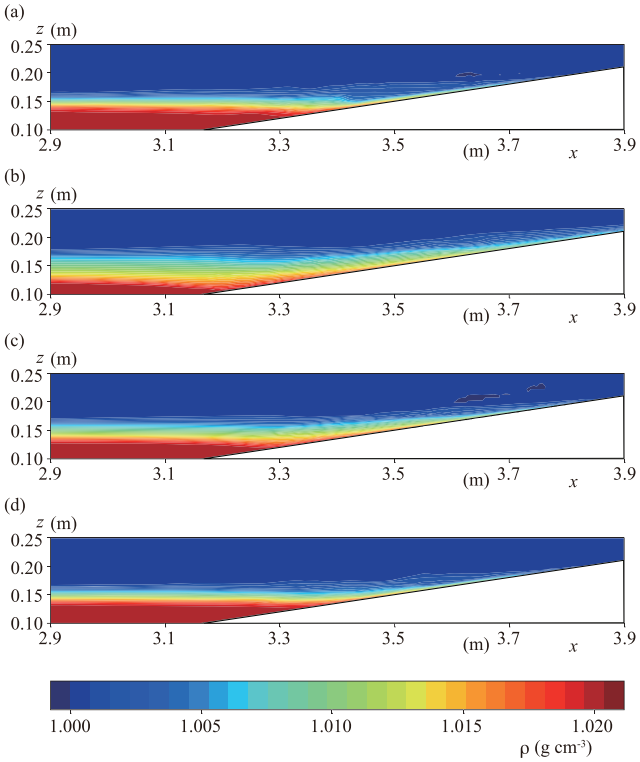

Figure 7. Phase-averaged density distribution for one IKW period at the lateral wall (a) Case A: no Coriolis effect, (b) Case B1: Coriolis coefficient of $4\pi/20$ s^{-1}, (c) Case B3: Coriolis coefficient of $4\pi/40$ s^{-1}, and (d) Case B5: Coriolis coefficient of $4\pi/160$ s^{-1}.

(residual undertow) to satisfy conservation of mass, as shown in Nakayama and Imberger (2010) (Figure 8a). When Coriolis was included, the residual current reached 0.03 m s^{-1} in Case B1, which was much larger than the no Coriolis case, because of energy concentration at the lateral wall. The residual current, around the phase-averaged pycnocline, due to breaking of the IKWs was found to be unidirectional, upslope from the offshore breaking point. The phase-averaged pycnocline elevation increased in the breaking zone (from $x = 3.4$ m to $x = 3.6$ m) with an increase in the Coriolis coefficient. Csanady (1975) theoretically demonstrated that IKWs play a substantial role in generating the observed coastal jets in Lake Ontario (Csanady, 1972a, 1972b). Valipour et al. (2019) also showed that coastal jets are caused in Lake Erie due to IKWs using field observations and a three-dimensional numerical model. In this study, we refer to the residual current generated through IKW breaking as a "residual jet" because the observed residual current is found to have the same unidirectional characteristics as the coastal jets.

To analyze the residual jet in more detail, residual currents at $z = 0.15$ m and 1 mm above the slope are shown in Figure 9. In Case A (no Coriolis), there was no change in the residual current in the spanwise direction (Figure 9a). However, a large difference in the spatial distribution of the residual current existed among all Coriolis cases (Figure 9b). In Case B3, the magnitude and direction of the residual current changed considerably in the spanwise direction, which resulted in the absence of strong residual current at $y = 0.2$ m at $z = 0.15$ m with the inertial deformation radius of 0.39 m. Also, the enhanced residual current was found to occur from $x = 3.2$ m to $x = 3.5$ m. Furthermore, in the residual current just above the slope, a downdraft was uniformly generated in the offshore direction without Coriolis (Figure 9c), but "oblique downdraft" occurred under Coriolis (Figure 9d). Additionally, the residual current from $x = 3.4$ m to $x = 3.5$ m over the slope, which corresponds to the region just below the pycnocline, was found to have oblique downdraft. The existence of the oblique downdraft, due to Coriolis, is expected to drive the residual jet around the phase-averaged pycnocline (Figure 8).

4. Discussion and Conclusions

The numerical simulations showed that the maximum velocity of the residual jet, u_B, that occurred in Case B1 was 3 times larger than that in Case B5 (Table 1). To understand this great effect of IKW breaking on the residual jet, we computed the phase-averaged (Eulerian averaged) velocity at the lateral wall without the effect of breaking by using U_{upper} and U_{lower} (Equations 2 and 3) numerically. It should be noted that the velocities plotted in Figure 10 were the vertically averaged velocities from $x = 3.4$ m to $x = 3.5$ m, where velocities are positive in Figure 8. It was found that the phase-averaged velocity, without IKW breaking, was much smaller than the residual jet, which suggests that the residual jet was induced by IKW breaking (Figure 10). In other words, there may be a possibility that IKW breaking enhances the speed of a residual jet adjacent to the lateral wall within the breaking zone. It is well known that such a phase-averaged current is associated with a mean surface elevation, in terms of the radiation stress, in the depth-integrated momentum flux (Longuet-Higgins & Stewart, 1962). The phase-averaged equilibrium momentum balance relation in the spanwise direction within the breaking zone, in the lower layer of a two-layer system, over the wave period is

$$\underbrace{\overline{\frac{\partial v_I}{\partial t} + u_I \frac{\partial v_I}{\partial x} + v_I \frac{\partial v_I}{\partial y}}}_{\text{negligible}} + \overline{f_C u_I} = -\overline{\varepsilon g \frac{\partial \eta_I}{\partial y}} - \underbrace{\overline{\frac{\rho_1}{\rho_2} g \frac{\partial \eta_S}{\partial y}}}_{\text{negligible}} \tag{6}$$

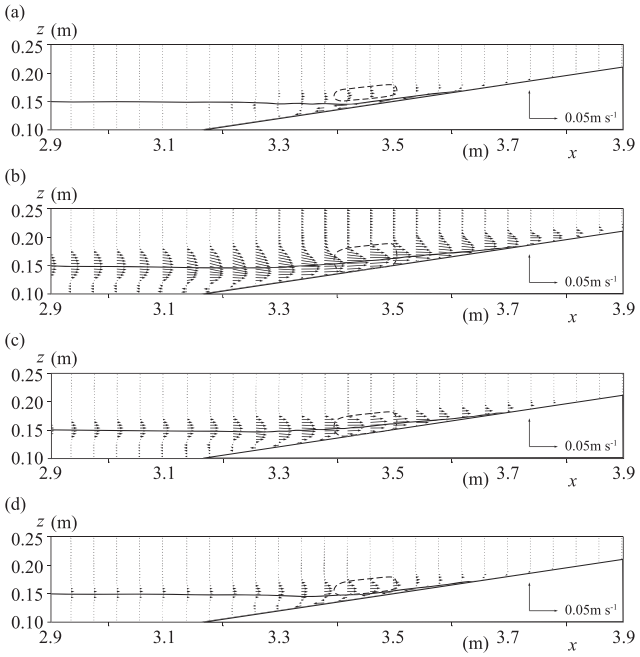

Figure 8. Residual current adjacent to the lateral wall. Solid lines indicate phase-averaged pycnocline elevation for one IKW. Dashed lines indicate the area to compute residual velocities. (a) Case A: no Coriolis effect, (b) Case B1: Coriolis coefficient of $4\pi/20$ s^{-1}, (c) Case B3: Coriolis coefficient of $4\pi/40$ s^{-1}, and (d) Case B5: Coriolis coefficient of $4\pi/160$ s^{-1}.

Here, the upper horizontal bar indicates the phase average, v_I is the velocity in the y direction in the lower layer, u_I is the velocity in the x direction in the lower layer, η_I is the pycnocline elevation, and η_S is the water surface elevation.

The phase-averaged advection term (the first to third terms of the left side) and the spanwise change in the phase-averaged surface elevation (the second term of the right side) in Equation 6 were confirmed to be negligible from the numerical simulations. By decomposing the pycnocline elevation and the flow velocity into components greater than and equal to the IKW period, $\eta_I = \overline{\eta} + \eta'$ (η' is the fluctuation of the pycnocline elevation from $\overline{\eta}$, and $\overline{\eta'} = 0$) and $u_I = u_B + u'$ (u' is the velocity fluctuation from u_B, and $\overline{u'} = 0$). Here, $\overline{\eta}$ and u_B are the phase-averaged pycnocline elevation and velocity, respectively, in the breaking zone adjacent to the lateral wall. Therefore, we obtain an equation to estimate the velocity of the residual jet, u_B.

$$f_C u_B = -\varepsilon g \frac{\partial \overline{\eta}}{\partial y}\bigg|_{lateral\ wall} \tag{7}$$

This approach is similar to the theoretical investigation of baroclinic currents by Csanady and Scott (1974) and Csanady (1975), in which a geostrophic balance was important for the generation of baroclinic currents. Charney (1955) also showed the occurrence of a coastal jet under the geostrophic balance.

A clear breaking zone was found in the range of $x = 3.4$ to 3.5 m (Figures 6 and 7), and we computed $\partial\overline{\eta}/\partial y$ at the lateral wall from the numerical simulations. As a result, the velocity of the residual jet from Equation 7 agrees with the numerical simulations, which shows that the geostrophic balance assumed in Equation 7 was established (Figure 10). Since it has been shown that a phase-averaged surface elevation drives mean flow under an external oscillatory force, such as radiation stress, the residual jet we obtained in this study is expected to be caused by an analogous effect, which is distinct in that Coriolis controls mean flow.

From the numerical simulations, it is possible to readily obtain the spatial distribution of a phase-averaged pycnocline, and so we applied Equation 7 to successfully estimate the velocity of the residual jet. However, it is difficult to measure the phase-averaged profile in the field. Therefore, we modify Equation 7 by introducing a new parameter, the effective pycnocline elevation at the lateral wall η_{B0}, and assuming that the gradient of $\overline{\eta}$ in the y direction is associated with η_{B0} and an inertial deformation radius, λ_I. The velocity of the residual jet, u_B, can be modeled as a function of η_{B0} when f_C and c_0 are constant (Equation 9).

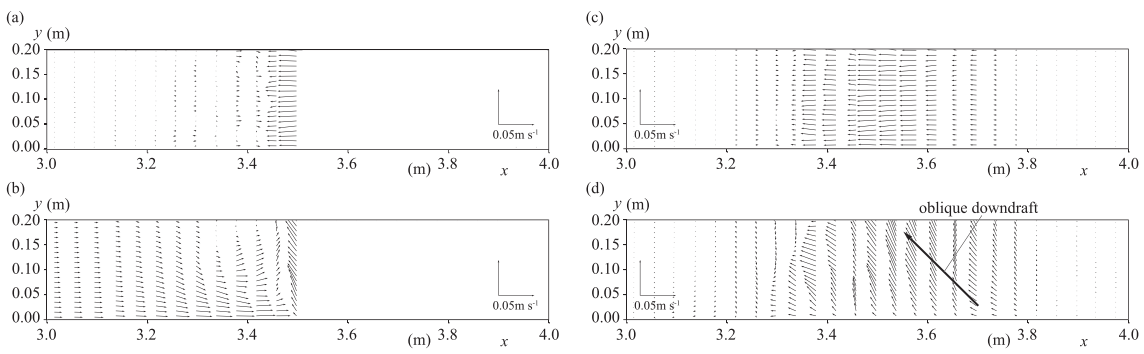

Figure 9. Residual current at $z = 0.15$ m of (a) Case A: without the Coriolis effect and (b) Case B3: with a Coriolis coefficient of $4\pi/40$ s^{-1}. Residual current adjacent to the slope of (c) Case A: no Coriolis effect and (d) Case B3: Coriolis coefficient of $4\pi/40$ s^{-1}.

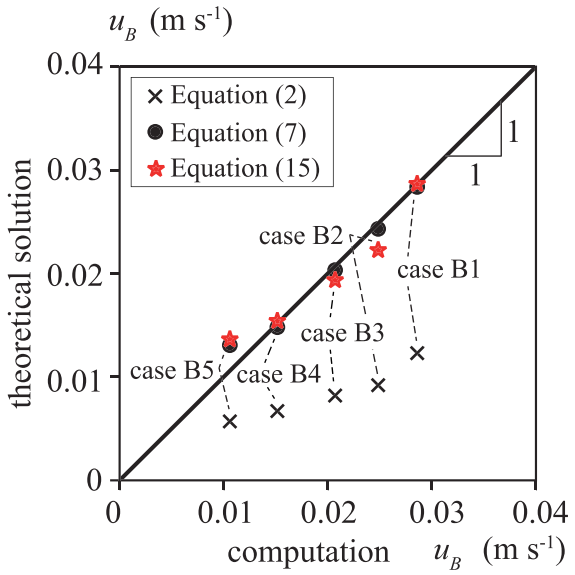

Figure 10. Comparisons of u_B between computations and theoretical solutions at $x = 3.5$ m.

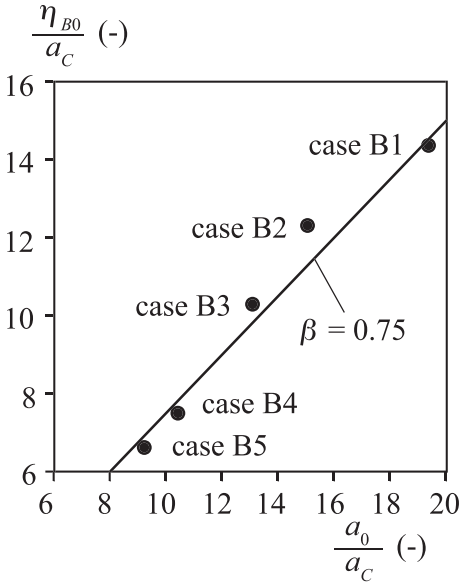

Figure 11. Relation between normalized amplitudes, a_0/a_C and η_{B0}/a_C, from numerical simulations for Cases B1 to B5. Solid lines indicate the best fit straight line.

$$\left.\frac{\partial\overline{\eta}}{\partial y}\right|_{lateral\ wall} = \frac{\partial}{\partial y}\left[\eta_{B0}\exp\left(-\frac{1}{\lambda_I}y\right)\right]_{lateral\ wall} = -\frac{\eta_{B0}}{\lambda_I} \tag{8}$$

$$u_B = \frac{\varepsilon g\eta_{B0}}{f_C\lambda_I} = \frac{\varepsilon g\eta_{B0}}{c_0} \tag{9}$$

where η_{B0} is the effective pycnocline elevation at the lateral wall.

The unknown parameter, η_{B0}, can be obtained by comparing Equations 7 and 9 as follows:

$$\eta_{B0} = -\frac{c_0\left.\partial\overline{\eta}\right|_{lateral\ wall}}{f_C\partial y} \tag{10}$$

Since the parameter, η_{B0}, is expected to be associated with turbulence, following Nakayama and Imberger (2010), we evaluated the critical amplitude, describing the strength of turbulence in internal wave breaking, to normalize the amplitude of the IKWs at the lateral wall and made comparisons with η_{B0} (Equation 11 and Figure 11):

$$a_C = C_S h_2 = \sqrt{\frac{8}{\pi B_P^5}}h_2 \tag{11}$$

$$B_P = \frac{2\omega_0}{f_S} \tag{12}$$

$$\omega_0 = \frac{2\pi t_0}{t_B} \tag{13}$$

$$t_0 = \frac{l_0}{\sqrt{\varepsilon g h_2}} \tag{14}$$

where a_C is the critical amplitude of internal wave breaking over a uniform slope, ω_0 is the normalized wave frequency of an internal incident wave, f_S is the breaking parameter over a uniform slope (= 0.9), t_B is the wave period of internal waves, l_0 is the horizontal length of a slope in the lower layer, and h_2 is the lower layer depth.

We found $a_C = 0.00126$ m, which is much smaller than the amplitude at the lateral wall, showing that in the absence of Coriolis the normalized amplitude $a_0/a_C = 8$, which means that reflection from the slope can be ignored (Nakayama & Imberger, 2010). In Case B5, where Coriolis was the smallest, the velocity of the residual jet was found to be almost the same as the offshore current in Case A (no Coriolis) (Figure 8). In other words, when turbulence due to IKW breaking occurs under conditions where λ_I is larger than the wavelength of the IKW (1.2 m), the geostrophic balance may be negligible in the phase-averaged field and consequently the residual jet becomes similar to the offshore current under the no Coriolis case. Melville et al. (1990) similarly demonstrated the importance of Coriolis when the Rossby radius was smaller than the wavelength of an IKW (Csanady, 1975). Also, it appears that η_{B0}/a_C is a linear function of a_0/a_C (Figure 11). Therefore, the velocity of residual jet may be estimated using the following equation when λ_I is equal to or smaller than the IKW wavelength.

$$u_B = \beta\frac{\varepsilon g a_0}{c_0} \tag{15}$$

where $\beta \sim 0.75$ from Figure 11. It should be noted that $\beta \sim 0.75$ was also obtained by giving the different amplitude, in which a_m is half as much

as Cases B1 to B5. Thus, there may be the possibility that $\beta \sim 0.75$ in the laboratory scale.

The proposed equations presented in this paper may allow predictions to be made for a residual jet in lakes and sea straits. As an example, we refer the results from a field study in Lake Erie by Valipour et al. (2019). They investigated two coastal jets generated by IKWs in Lake Erie by deploying acoustic doppler current profilers and thermistor chains. One was a westward coastal jet with a phase speed of 0.37 m s^{-1} in the eastern basin, and the other is also a westward coastal jet with a phase speed of 0.22 m s^{-1} in the central basin. The specific density difference was about 0.0029 between a 5°C hypolimnion and 25°C epilimnion. The Estuary and Lake Computer Model (ELCOM) was applied to estimate the velocity of the coastal jets to be ~0.3 m s^{-1} in the eastern basin and ~0.2 m s^{-1} in the shallower central basin. Valipour et al. (2015) measured the displacement of pycnocline in the central basin of Lake Erie to be < ~5 m. We may thus use Equation 15 to estimate the velocity of a residual jet in the central basin to be $u_B = 0.10$, 0.20, and 0.30 m s^{-1} when the phase speed is 0.22 m s^{-1} and the amplitudes of IKWs are 1.0, 2.0, and 3.0 m, respectively, which reasonably agree with the velocity of the coastal jets from ELCOM, 0.2 m s^{-1}. But the computed velocity of the coastal jets by ELCOM was also similar to the linear baroclinic phase speed. Also, Valipour et al. (2019) does not show the importance of the breaking effect of IKWs though ELCOM can include the effect of the breaking of IKWs. Therefore, further research is needed to confirm the generation mechanisms energizing coastal jets and the parameter β in a real scale.

Experiments on breaking of IKWs over a slope using a rotating tank showed that the presence of the Coriolis force drives collapsing-surging breakers adjacent to the lateral wall. The type of breaking changed, in the spanwise direction, when the depths of the upper and lower layers were the same, although collapsing breakers dominated when Coriolis was neglected. Using a three-dimensional DNS model, a residual jet was shown to occur adjacent to the lateral wall on the right side of the progressive IKWs under Coriolis. The residual jet was found to be driven by an oblique downdraft running down the slope due to Coriolis. Therefore, in addition to the existing theory on known mechanisms, a new mechanism to generate residual jets was proposed in this study characterized by IKW breaking.

Furthermore, an equation for estimating the residual current, due to the jet, was formulated; it was demonstrated that the normalized amplitude (a_0/a_C) has a value of about 0.5 to 20 at field scale (Nakayama & Imberger, 2010). It is possible for the range of (a_0/a_C) to be from 6 to 20, to predict the occurrence of the residual jet, which may control long-term mass transport, using Equation 15. Therefore, even when the thicknesses of the upper and lower layers are the same, it is important to collect additional data, in future, with different Coriolis coefficients and normalized amplitudes to verify Equation 15 for predicting u_B using f_C, a_0/a_C, and η_{B0}, especially the case when a_0/a_C is from 0.5 to 6.0. Additionally, in the future, it is necessary to investigate the long-term mass transport due to IKWs under different upper- and lower-layer thicknesses.

Data Availability Statement

The executable binary (windows, Mac, and Linux) of the three-dimensional hydrodynamic model, Fantom, used in this study, is available online (http://www.comp.tmu.ac.jp/shintani/fantom.html). The model outputs are available from http://doi.org/10.5281/zenodo.3900023, "The model outputs for Nakayama et al. (2019)."

Acknowledgments
This work was supported by the Japan Society for the Promotion of Science under Grants 18H01545 and 18KK0119. We thank Y. Watanabe and Shimizu, K. for helpful comments.

References

Adcroft, A. J., Hill, C. N., & Marshall, J. (1997). Representation of topography by shaved cells in a height coordinate ocean model. *Monthly Weather Review*, *125*(9), 2293–2315. https://doi.org/10.1175/1520-0493(1997)125<2293:ROTBSC>2.0.CO;2

Aghsaee, P., & Boegman, L. (2015). Experimental investigation of sediment resuspension beneath internal solitary waves of depression. *Journal of Geophysical Research: Oceans*, *120*, 3301–3314. https://doi.org/10.1002/2014JC010401

Aghsaee, P., Boegman, L., & Lamb, K. G. (2010). Breaking of shoaling internal solitary waves. *Journal of Fluid Mechanics*, *659*, 289–317. https://doi.org/10.1017/S002211201000248X

Antenucci, J. P., & Imberger, J. (2001). Energetics of long internal gravity waves in large lakes. *Limnology and Oceanography*, *46*(7), 1760–1773. https://doi.org/10.4319/lo.2001.46.7.1760

Arthur, R. S., & Fringer, O. B. (2014). The dynamics of breaking internal solitary waves on slopes. *Journal of Fluid Mechanics*, *761*, 360–398. https://doi.org/10.1017/jfm.2014.641

Asplin, L., Salvanes, A. G. V., & Kristoffersen, J. B. (1999). Nonlocal wind-driven fjord–coast advection and its potential effect on plankton and fish recruitment. *Fisheries Oceanography*, *8*(4), 255–263. https://doi.org/10.1046/j.1365-2419.1999.00109.x

Boegman, L., Imberger, J., Ivey, G. N., & Antenucci, J. P. (2003). High-frequency internal waves in large stratified lakes. *Limnology and Oceanography*, *48*(2), 895–919. https://doi.org/10.4319/lo.2003.48.2.0895

Boegman, L., & Ivey, G. N. (2009). Flow separation and resuspension beneath shoaling nonlinear internal waves. *Journal of Geophysical Research*, *114*, C02018. https://doi.org/10.1029/2007JC004411

Boegman, L., Ivey, G. N., & Imberger, J. (2005a). The degeneration of internal waves in lakes with sloping topography. *Limnology and Oceanography*, *50*(5), 1620–1637. https://doi.org/10.4319/lo.2005.50.5.1620

Boegman, L., Ivey, G. N., & Imberger, J. (2005b). The energetics of large-scale internal wave degeneration in lakes. *Journal of Fluid Mechanics*, *531*, 159–180. https://doi.org/10.1017/S0022112005003915

Boegman, L., & Stastna, M. (2019). Sediment resuspension and transport by internal solitary waves. *Annual Review of Fluid Mechanics*, *51*(1), 129–154. https://doi.org/10.1146/annurev-fluid-122316-045049

Bourgault, D., Morsilli, M., Richards, C., Neumeier, U., & Kelley, D. E. (2014). Sediment resuspension and nepheloid layers induced by long internal solitary waves shoaling orthogonally on uniform slopes. *Continental Shelf Research*, *72*, 21–33. https://doi.org/10.1016/j.csr.2013.10.019

Charney, J. G. (1955). The generation of oceanic currents by the wind. *Journal of Marine Research*, *14*, 477–498. Retrieved from https://images.peabody.yale.edu/publications/jmr/jmr14-04-20.pdf

Csanady, G. T. (1967). Large-scale motion in the great lakes. *Journal of Geophysical Research*, *72*(16), 4151–4162. https://doi.org/10.1029/JZ072i016p04151

Csanady, G. T. (1972a). The coastal boundary layer in Lake Ontario: Part II. The summer-fall regime. *Journal of Physical Oceanography*, *2*(2), 168–176. https://doi.org/10.1175/1520-0485(1972)002<0166:TCBLIL>2.0.CO;2

Csanady, G. T. (1972b). The coastal boundary layer in Lake Ontario. Part I: The spring regime. *Journal of Physical Oceanography*, *2*, 41–53. https://doi.org/10.1175/1520-0485(1972)002<0041:TCBLIL>2.0.CO;2

Csanady, G. T. (1975). Hydrodynamics of large lakes. *Annual Review of Fluid Mechanics*, *7*(1), 357–386. https://doi.org/10.1146/annurev.fl.07.010175.002041

Csanady, G. T., & Scott, J. T. (1974). Baroclinic coastal jets in Lake Ontario during IFYGL. *Journal of Physical Oceanography*, *4*(4), 524–541. https://doi.org/10.1175/1520-0485(1974)004<0524:BCJILO>2.0.CO;2

Davis, K. A., & Monismith, S. G. (2011). The modification of bottom boundary layer turbulence and mixing by internal waves shoaling on a barrier reef. *Journal of Physical Oceanography*, *41*(11), 2223–2241. https://doi.org/10.1175/2011JPO4344.1

de la Fuente, A., Shimizu, K., Imberger, J., & Niño, Y. (2008). The evolution of internal waves in a rotating, stratified, circular basin and the influence of weakly nonlinear and nonhydrostatic accelerations. *Limnology and Oceanography*, *53*(6), 2738–2748. https://doi.org/10.4319/lo.2008.53.6.2738

Derzho, O. G., & Grimshaw, R. (1997). Solitary waves with a vortex core in a shallow layer of stratified fluid. *Physics of Fluids*, *9*(11), 3378–3385. https://doi.org/10.1063/1.869450

Fujita, I. (2002). Particle image analysis of open-channel flow at a backward facing step having a trench. *Journal of Visualization*, *5*(4), 335–342. https://doi.org/10.1007/BF03182348

Fujita, I., & Maruyama, T. (2002). Hydraulic characteristics of open-channel flow downstream of a drop structure having a trench. *Journal of Hydroscience and Hydraulic Engineering*, *20*(1), 103–111.

Galvin, C. J. (1968). Breaker type classification on three laboratory beaches. *Journal of Geophysical Research*, *73*(12), 3651–3659. https://doi.org/10.1029/JB073i012p03651

Gill, A. (1982). *Atmosphere-ocean dynamics* (Vol. 30, p. 662). New York: Academic Press. Retrieved from https://www.elsevier.com/books/atmosphere-ocean-dynamics/gill/978-0-12-283522-3

Gloor, M., Wüest, A., & Münnich, M. (1994). Benthic boundary mixing and resuspension induced by internal seiches. *Hydrobiologia*, *284*(1), 59–68. https://doi.org/10.1007/BF00005731

Grimshaw, R., Guo, C., Helfrich, K. R., & Johnson, E. R. (2013). Experimental study of the effect of rotationon nonlinear internal waves. *Physics of Fluids*, *25*(5), 056602. https://doi.org/10.1063/1.4805092

Grimshaw, R., Guo, C., Helfrich, K. R., & Vlasenko, V. (2014). Combined effect of rotation and topography on shoaling oceanic internal solitary waves. *Journal of Physical Oceanography*, *44*(4), 1116–1132. https://doi.org/10.1175/JPO-D-13-0194.1

Grimshaw, R., & Helfrich, K. R. (2012). The effect of rotation on internal solitary waves. *IMA Journal of Applied Mathematics*, *77*(3), 326–339. https://doi.org/10.1093/imamat/hxs024

Hamblin, P. F. (1978). Internal Kelvin waves in a Fjord lake. *Journal of Geophysical Research*, *83*(C5), 2409–2418. https://doi.org/10.1029/JC083iC05p02409

Helfrich, K. R. (1992). Internal solitary wave breaking and run-up on a uniform slope. *Journal of Fluid Mechanics*, *243*(1), 133–154. https://doi.org/10.1017/s0022112092002660

Helfrich, K. R. (2007). Decay and return of internal solitary waves with rotation. *Physics of Fluids*, *19*(2), 026601. https://doi.org/10.1063/1.2472509

Helfrich, K. R., & Melville, W. K. (2006). Long nonlinear internal waves. *Annual Review of Fluid Mechanics*, *38*(1), 395–425. https://doi.org/10.1146/annurev.fluid.38.050304.092129

Helfrich, K. R., Melville, W. K., & Miles, J. W. (1984). On interfacialsolitary waves over slowly varying topography. *Journal of Fluid Mechanics*, *149*(1), 305–317. https://doi.org/10.1017/S0022112084002664

Horn, D. A., Imberger, J., & Ivey, G. N. (2001). The degeneration of large-scale interfacial gravity waves in lakes. *Journal of Fluid Mechanics*, *434*, 181–207. https://doi.org/10.1017/S0022112001003536

Horn, D. A., Imberger, J., Ivey, G. N., & Redekopp, L. G. (2002). A weakly nonlinear model of long internal waves in closed basins. *Journal of Fluid Mechanics*, *467*, 269–287. https://doi.org/10.1017/S0022112002001362

Horn, D. A., Redekopp, L. G., Imberger, J., & Ivey, G. N. (2000). Internal wave evolution in a space-time varying field. *Journal of Fluid Mechanics*, *424*, 279–301. https://doi.org/10.1017/S0022112000001841

Hosegood, P., Bonnin, J., & van Haren, H. (2004). Solibore-induced sediment resuspension in the Faeroe-Shetland Channel. *Geophysical Research Letters*, *31*, L09301. https://doi.org/10.1029/2004GL019544

Inall, M. E. (2009). Internal wave induced dispersion and mixing on a sloping boundary. *Geophysical Research Letters*, *36*, L05604. https://doi.org/10.1029/2008GL036849

Jones, W. P., & Launder, B. E. (1972). The prediction of laminarization with a two-equation model of turbulence. *International Journal of Heat and Mass Transfer*, *15*(2), 301–314. https://doi.org/10.1016/0017-9310(72)90076-2

Klymak, J. M., & Moum, J. N. (2003). Internal solitary waves of elevation advancing on a shoaling shelf. *Geophysical Research Letters*, *30*(20), 2045. https://doi.org/10.1029/2003GL017706

Lamb, K. G. (2002). A numerical investigation of solitary internal waves with trapped cores formed via shoaling. *Journal of Fluid Mechanics*, *451*, 109–144. https://doi.org/10.1017/S002211200100636X

Lamb, K. G. (2014). Internal wave breaking and dissipation mechanisms on the continental slope/shelf. *Annual Review of Fluid Mechanics*, *46*(1), 231–254. https://doi.org/10.1146/annurev-fluid-011212-140701

Longuet-Higgins, M. S., & Stewart, R. W. (1962). Radiation stress and mass transport in gravity waves, with application to 'surf beats'. *Journal of Fluid Mechanics*, *13*(4), 481–504. https://doi.org/10.1017/S0022112062000877

Maruya, Y., Nakayama, K., Shintani, T., & Yonemoto, M. (2010). Evaluation of entrainment velocity induced by wind stress in a two-layer system. *Hydrological Research Letters*, *4*, 70–74. https://doi.org/10.3178/hrl.4.70

Maxworthy, T. (1983). Experiments on solitary internal Kelvin waves. *Journal of Fluid Mechanics*, *129*(1), 365–383. https://doi.org/10.1017/S0022112083000816

Melville, W. K., Tomasson, G. G., & Renouard, D. P. (1989). On the stability of Kelvin waves. *Journal of Fluid Mechanics*, *206*, 1–23. https://doi.org/10.1017/S002211208900220X

Melville, W. K., Renouard, D. P., & Zhang, X. (1990). On the generation of nonlinear internal Kelvin waves in a rotating channel. *Journal of Geophysical Research*, *95*(C10), 18,247–18,254. https://doi.org/10.1029/jc095ic10p18247

Moin, P., & Mahesh, K. (1998). Direct numerical simulation: A tool in turbulence research. *Annual Review of Fluid Mechanics*, *30*(1), 539–578. https://doi.org/10.1146/annurev.fluid.30.1.539

Mortimer, C. H. (1952). Water movements in lakes during summer stratification: Evidence from the distribution of temperature in Windemere. *Philosophical Transactions of the Royal Society A: Mathematical, Physical and Engineering Sciences*, *236*, 355–404. https://doi.org/10.1098/rstb.1952.0005

Mortimer, C. H. (2004). *Lake Michigan in motion: Responses of an inland sea to weather, Earth-spin, and human activities*. Wisconsin: University of Wisconsin Press. Retrieved from https://uwpress.wisc.edu/books/3132.htm

Moum, J. N., Farmer, D. M., Smyth, W. D., Armi, L., & Vagle, S. (2003). Structure and generation of turbulence at interfaces strained by internal solitary waves propagating shoreward over the continental shelf. *Journal of Physical Oceanography*, *33*(10), 2093–2112. https://doi.org/10.1175/1520-0485(2003)033<2093:SAGOTA>2.0.CO;2

Nakamoto, A., Nakayama, K., Shintani, T., Maruya, Y., Komai, K., Ishida, T., & Makiguchi, Y. (2013). Adaptive management in Kushiro wetland in the context of salt wedge intrusion due to sea level rise. *Hydrological Research Letters*, *7*(1), 1–5. https://doi.org/10.3178/hrl.7.1

Nakayama, K., & Imberger, J. (2010). Residual circulation due to internal waves shoaling on a slope. *Limnology and Oceanography*, *55*(3), 1009–1023. https://doi.org/10.4319/lo.2010.55.3.1009

Nakayama, K., Kakinuma, T., & Tsuji, H. (2019). Oblique reflection of large internal solitary waves in a two-layer fluid. *European Journal of Mechanics - B/Fluids*, *74*, 81–91. https://doi.org/10.1016/j.euromechflu.2018.10.014

Nakayama, K., Nguyen, H. D., Shintani, T., & Komai, K. (2016). Reversal of secondary circulations in a sharp channel bend. *Coastal Engineering Journal*, *58*. https://doi.org/10.1142/S0578563416500029

Nakayama, K., Sato, T., Shimizu, K., & Boegman, L. (2019). Classification of internal solitary wave breaking over a slope. *Physical Review Fluids*, *4*(1), 014801. https://doi.org/10.1103/PhysRevFluids.4.014801

Nakayama, K., Shintani, T., Kokubo, K., Kakinuma, T., Maruya, Y., Komai, K., & Okada, T. (2012). Residual current over a uniform slope due to breaking of internal waves in a two-layer system. *Journal of Geophysical Research*, *117*, C10002. https://doi.org/10.1029/2012JC008155

Nakayama, K., Shintani, T., Komai, K., Nakagawa, Y., Tsai, J. W., Sasaki, D., et al. (2020). Integration of submerged aquatic vegetation motion within hydrodynamic models. *Water Resources Research*, *56*, 027369. https://doi.org/10.1029/2020WR027369

Nakayama, K., Shintani, T., Shimizu, K., Okada, T., Hinata, H., & Komai, K. (2014). Horizontal and residual circulations driven by wind stress curl in Tokyo Bay. *Journal of Geophysical Research: Oceans*, *119*, 1977–1992. https://doi.org/10.1002/2013JC009396

Pierson, D. C., & Weyhenmeyer, G. A. (1994). High resolution measurements of sediment resuspension above an accumulation bottom in a stratified lake. *Hydrobiologia*, *284*(1), 43–57. https://doi.org/10.1007/BF00005730

Pineda, J. (1994). Internal tidal bores in the nearshore: Warm-water fronts, seaward gravity currents and the onshore transport of neustonic larvae. *Journal of Marine Research*, *52*(3), 427–458. https://doi.org/10.1357/0022240943077046

Reeder, D. B., Ma, B. B., & Yang, Y. J. (2011). Very large subaqueous sand dunes on the upper continental slope in the South China Sea generated by episodic, shoaling deep-water internal solitary waves. *Marine Geology*, *279*(1–4), 12–18. https://doi.org/10.1016/j.margeo.2010.10.009

Renouard, D. P., D'Hières, G. C., & Zhang, X. (1987). An experimental study of strongly nonlinear waves in a rotating system. *Journal of Fluid Mechanics*, *177*, 381–394. https://doi.org/10.1017/S0022112087001009

Sandstrom, H., & Elliott, J. A. (1984). Internal tide and solitons on the Scotian Shelf: A nutrient pump at work. *Journal of Geophysical Research*, *89*(C4), 6415–6426. https://doi.org/10.1029/jc089ic04p06415

Scotti, A., & Pineda, J. (2004). Observation of very large and steep internal waves of elevation near the Massachusetts coast. *Geophysical Research Letters*, *31*, L22307. https://doi.org/10.1029/2004GL021052

Shimizu, K., & Nakayama, K. (2017). Effects of topography and earth's rotation on the oblique interaction of internal solitary-like waves in the Andaman Sea. *Journal of Geophysical Research: Oceans*, *122*, 7449–7465. https://doi.org/10.1002/2017JC012888

Steinman, B., Eckert, W., Kaganowsky, S., & Zohary, T. (1997). Seiche-induced resuspension in Lake Kinneret: A fluorescent tracer experiment. *Water, Air, & Soil Pollution*, *99*(1–4), 123–131. https://doi.org/10.1007/BF02406851

Stocker, R., & Imberger, J. (2003). Energy partitioning and horizontal dispersion in a stratified rotating lake. *Journal of Physical Oceanography*, *33*(3), 512–529. https://doi.org/10.1175/1520-0485(2003)033<0512:EPAHDI>2.0.CO;2

Sutherland, B. R., Barrett, K. J., & Ivey, G. N. (2013). Shoaling internal solitary waves. *Journal of Geophysical Research: Oceans*, *118*, 4111–4124. https://doi.org/10.1002/jgrc.20291

Thorpe, S. A. (1978). On the shape and breaking of finite amplitude internal gravity waves in a shear flow. *Journal of Fluid Mechanics*, *85*(1), 7–31. https://doi.org/10.1017/S0022112078000518

Ulloa, H. N., Winters, K. B., de la Fuente, A., & Niño, Y. (2015). Degeneration of internal Kelvin waves in a continuous two-layer stratification. *Journal of Fluid Mechanics*, *777*, 68–96. https://doi.org/10.1017/jfm.2015.311

Umlauf, L., & Burchard, H. (2003). A generic length-scale equation for geophysical turbulence models. *Journal of Marine Research*, *61*(2), 235–265. https://doi.org/10.1357/002224003322005087

Valipour, R., Bouffard, D., Boegman, L., & Rao, Y. R. (2015). Near-inertial waves in Lake Erie. *Limnology and Oceanography*, *60*(5), 1522–1535. https://doi.org/10.1002/lno.10114

Valipour, R., Rao, Y. R., León, L. F., & Depew, D. (2019). Nearshore-offshore exchanges in multi-basin coastal waters: Observations and three-dimensional modeling in Lake Erie. *Journal of Great Lakes Research*, *45*(1), 50–60. https://doi.org/10.1016/j.jglr.2018.10.005

Wake, G. W., Ivey, G. N., & Imberger, J. (2005). The temporal evolution of baroclinic basin-scale waves in a rotating circular basin. *Journal of Fluid Mechanics*, *523*, 367–392. https://doi.org/10.1017/S0022112004002344

Walter, R. K., Woodson, C. B., Arthur, R. S., Fringer, O. B., & Monismith, S. G. (2012). Nearshore internal bores and turbulent mixing in southern Monterey Bay. *Journal of Geophysical Research*, *117*, C07017. https://doi.org/10.1029/2012JC008115

Wüest, A., & Lorke, A. (2003). Small-scale hydrodynamics in lakes. *Annual Review of Fluid Mechanics*, *35*(1), 373–412. https://doi.org/10.1146/annurev.fluid.35.101101.161220